

Skull Diversity and Evolution in Miniaturized Amphibians, Genus *Brachycephalus* (Anura: Brachycephalidae)

Sérgio F. dos Reis¹ | Rute B. G. Clemente-Carvalho² | Caio M. S. F. F. dos Santos³ | Ricardo T. Lopes³ | Fernando J. Von Zuben⁴ | Prianda R. Laborda¹ | S. Ivan Perez⁵

¹Departamento de Biologia Animal, Universidade Estadual de Campinas, Campinas, São Paulo, Brazil

²Department of Biology, Queen's University, Kingston, Ontario, Canada; Hakai Institute/Tula Foundation, Harriot Bay, British Columbia, Canada (present address)

³Laboratório de Instrumentação Nuclear, Programa de Engenharia Nuclear, Universidade Federal do Rio de Janeiro/COPPE, Rio de Janeiro, Brazil

⁴Departamento de Engenharia de Computação e Automação Industrial, Universidade Estadual de Campinas, Campinas São Paulo, Brazil

⁵División Antropología, Facultad de Ciencias Naturales y Museo (FCNyM, UNLP), Consejo Nacional de Investigaciones Científicas y Técnicas, La Plata, Argentina

Correspondence

¹Departamento de Biologia Animal, Instituto de Biologia, Universidade Estadual de Campinas, Campinas, São Paulo, 13083-970, Brazil

+55(019)3521-6279; E-mail: sfreis@unicamp.br

Running title: Skull diversity in miniaturized *Brachycephalus*

This article has been accepted for publication and undergone full peer review but has not been through the copyediting, typesetting, pagination and proofreading process which may lead to differences between this version and the Version of Record. Please cite this article as doi: 10.1002/ar.24554

Grant sponsors: Fundação de Amparo à Pesquisa do Estado de São Paulo, Coordenação de Aperfeiçoamento de Pessoal de Nível Superior; Grant numbers: 2017/17357-0, Finance Code 001.

Abstract

Miniaturized amphibians of the genus *Brachycephalus* are phenotypically diverse. The species of *Brachycephalus* have bufoniform or leptodactyliiform baupläne and any of three skeletal states: non-hyperossified, hyperossified without dorsal shield, and hyperossified with dorsal shield. We integrate high-resolution microcomputed tomography, geometric morphometrics, and an estimate of molecular phylogenetic relationships to investigate skull diversity in shape and size-shape space in selected species of *Brachycephalus*. Skull diversity amongst species of *Brachycephalus* can be partitioned into shape and size-shape space according to the four conditions of skeletal states-baupläne, namely, non-hyperossified leptodactyliiform, non-hyperossified bufoniform, hyperossified bufoniform without dorsal shield, and hyperossified bufoniform with dorsal shield. Skull diversity in shape and size-shape space in non-hyperossified leptodactyliiform species of *Brachycephalus* is markedly larger, when compared to skull diversity in species of the three other conditions of skeletal states-baupläne. Variation in skull shape scales with size across *Brachycephalus* and, therefore, can be explained by allometry. Skull diversity, baupläne, and skeletal states covary to a large extent with monophyletic lineages of *Brachycephalus*, as revealed by a mitochondrial DNA species tree. Non-hyperossified bufoniform species and hyperossified bufoniform species with or without dorsal shield are monophyletic lineages, as inferred from a mitochondrial DNA species tree. Non-hyperossified leptodactyliiform species of *Brachycephalus* do not share, however, a most recent common ancestor. The non-hyperossified leptodactyliiform species of *Brachycephalus*, due to their marked skull diversity and lack of monophyly, emerge as evolutionarily complex. Therefore, further sampling of the non-hyperossified leptodactyliiform condition of skeletal states-baupläne will be necessary to further understand the evolutionary history of *Brachycephalus*.

KEYWORDS

Allometry, Brazilian Atlantic Forest, geometric morphometrics, hyperossification,
mitochondrial DNA species tree, shape space, size-shape space, skull

1 | INTRODUCTION

Amphibians of the genus *Brachycephalus* are amongst the smallest vertebrates in the world. Currently, thirty-six species are described for the genus *Brachycephalus*, which occurs in the Atlantic Forest from Northeast to Southern Brazil (Condez et al., 2020; Frost, 2020). Externally, the species of *Brachycephalus* have one of two baupläne (Handigran and Wassersug, 2007), that is, a common, basic organizational plan: bufoniform (toad-like) or leptodactyliform (frog-like, Fig. 1). The bufoniform/leptodactyliform baupläne are defined comparatively as follows (Condez et al., 2014, 2016): body robust/slender, pectoral girdle robust/slender, head as wide as long/wider than long, snout short/long. The bufoniform species of *Brachycephalus* amount to 32 taxa, with several additional species still unnamed (Condez et al., 2020). Four species of leptodactyliform *Brachycephalus* have been described and several others remain undescribed (Napoli et al., 2011; Condez et al., 2020). Bufoniform species vary markedly in body coloration, whereas leptodactyliform species are brownish in color (Fig. 1). *Brachycephalus* is at the lowest limit of vertebrate size, ranging from 8.6 to 19.0 mm in body size. The smallest species of *Brachycephalus* are near in size to the smallest known vertebrate, the frog *Paedophryne amauensis* from New Guinea, which attains an average body size of 7.7 mm (Rittmeyer et al., 2012).

The dramatic reduction in body size in *Brachycephalus* is the outcome of miniaturization, an evolutionary process by which extremely small body size in a lineage arises from a larger ancestor (Hanken and Wake, 1993). Whereas there is not a critical size that defines miniaturization on theoretical or biological criteria (Hanken and Wake, 1993), it is widely accepted that amphibians < 20 mm in body size are miniaturized (Clarke, 1996). *Brachycephalus* is therefore miniaturized given this threshold in body size. An evolutionary novelty, a hyperossified dorsal shield, did arise in some bufoniform species of *Brachycephalus* (Hanken, 1993; Clemente-Carvalho et al., 2009). Hyperossification, an increased mineralization and excessive ossification, is a prominent feature of the skeleton of some bufoniform species (Trueb,

1973; Trueb and Alberch, 1985; Hanken, 1993; Clemente-Carvalho et al., 2009). Three skeletal states evolved in *Brachycephalus*, namely, non-hyperossified, hyperossified without dorsal shield, and hyperossified with dorsal shield (Clemente-Carvalho et al., 2009). Non-hyperossified species lack bone sculpturing in the skull, spinal processes of sacral, and presacral vertebrae (Clemente-Carvalho et al., 2009). Hyperossified species have bone sculpturing, which appears macroscopically as ridges and crests inducing a reticulated or pitted pattern in the skull, spinal processes of sacral, and presacral vertebrae (Clemente-Carvalho et al., 2009). The dorsal shield is also sculptured (Clemente-Carvalho et al., 2009).

Morphological diversity such as that observed in complex structures like the skull can be measured qualitatively in terms of variation in phenotypic states and, quantitatively, in terms of the association between size and shape within the context of allometry, which explains how changes in size extrapolate to changes in shape (Klingenberg, 2016). A fundamental task is therefore to determine the extent to which morphological diversity is associated with molecular phylogenetic relationships. Here, we apply these concepts to investigate skull diversity in selected species of *Brachycephalus*. We chose the skull because this structure is a vertebrate novelty that houses the brain and specialized sensory organs (Fish, 2017; Yang and Ornitz, 2019). Specifically, our objectives were the following. First, we use virtual surfaces derived from high-resolution microcomputed tomography to characterize the three skeletal states and their distribution across the species of *Brachycephalus* sampled here. Second, we use three-dimensional geometric morphometrics (3DGM; Cardini, 2020; Mitteroecker, 2020) to characterize skull diversity in *Brachycephalus* in ordinated shape space (Mitteroecker, 2020). From a geometric perspective, the scale of description of shape is determined by the density of points, registered as Cartesian coordinates, sampled from individual phenotypes. We used the virtual surfaces to manually register points, defined as landmarks and curve and surface semilandmarks, which yield a limited number of coordinates (Gao et al., 2018). We also used a

fully automated method of registration of coordinates, which yields tens of thousands of coordinates (Pomidor et al., 2016). Third, we further quantify the diversity in the skull of *Brachycephalus* in ordinated size-shape space within the framework of allometry (Mitteroecker et al., 2004). Fourth, we use mitochondrial DNA sequences to compute a species tree to estimate ancestor-descendant relationships in *Brachycephalus* under the formalism of the multi-species coalescent model (Rannala et al., 2020).

2 | MATERIAL AND METHODS

2.1 | Taxon sampling

The species of *Brachycephalus* have one of two baupläne, bufoniform or leptodactyliform. Each species of *Brachycephalus* examined here was classified as either bufoniform or leptodactyliform based on definitions of these baupläne and/or information in the original descriptions. Each species was also classified to a skeletal state, namely, non-hyperossified, hyperossified without dorsal shield, or hyperossified with dorsal shield, based on the reconstructed tomographic surfaces. Given the baupläne and the skeletal states there are four conditions to which a species of *Brachycephalus* can be assigned to, namely, non-hyperossified leptodactyliform, non-hyperossified bufoniform, hyperossified bufoniform without dorsal shield, and hyperossified bufoniform with dorsal shield. Taxon sampling of *Brachycephalus* aimed at morphological and molecular analyses should include species representative of each of these four conditions, and we sampled 18 species spanning the four conditions of skeletal states-baupläne. For the morphological analyses we sampled 55 alcohol-preserved specimens of 18 species of *Brachycephalus* of each three skeletal states. For the molecular analyses we had access to tissue samples of the following species of the four skeletal states-baupläne conditions. Non-hyperossified leptodactyliform: *B. didactylus*, *B. hermogenesi*, and *B. pulex*; non-hyperossified bufoniform: *B. brunneus*, *B. ferruginus*, *B. izecksohni*, *B. pernix*, and *B. pombali*; hyperossified bufoniform without dorsal shield: *B. alipioi*, *B. crispus*, *B. guarani*, *B. nodoterga*, *B. pitanga*, *B. vertebralis*, and hyperossified bufoniform with dorsal shield: *B. toby*; and *B. ephippium*, *B. garbeanus*, and *B. margaritatus*. Information on samples sizes, localities, and geographic coordinates are given in Table 1. Taxonomic identification of species was based on morphological information provided in the original descriptions. The specimens analyzed here are deposited in the collections of the Museu Nacional, Rio de Janeiro; Universidade Estadual de Santa Cruz, Bahia; Coleção Célio Haddad, Universidade Estadual Paulista, Rio Claro, São

Paulo; and Museu de Zoologia da Universidade Estadual de Campinas “Adão José Cardoso”, São Paulo, Brazil.

2.2 | Virtual reconstruction of skeletal diversity from 3D microcomputed tomography

High resolution three-dimensional (3D) microcomputed tomography images of museum preserved skeletons of *Brachycephalus* were made using the Phoenix V|tomex|300 M GE tomography system at the Laboratório de Instrumentação Nuclear at COPPE, Universidade Federal do Rio de Janeiro, Rio de Janeiro, Brazil. The parameters for image acquisition were as follows: 55 kV voltage and 250 μ A current for each frame. We made an average of five frames (skipping 2), with 250 ms exposure time and a total of 1200 projections with pixel size within the range of 13 μ m to 18 μ m per scan. Three-dimensional reconstructions of individual *Brachycephalus* skeletons were made using the software Phoenix Datos/X v. 2.2 (GE). The threshold-based and manual segmentation was performed with the AVIZO software (AVIZO Fire 9.1). Images were saved as polygon (.ply) files. According to Pomidor et al. (2016), to generate surfaces from tomographic images individual specimens must be the most complete, the most representative, and the most morphologically atypical in the sample. We made tomographic images of several specimens per species, digitally reconstructed the skull, and retained only individuals that met the three criteria defined by Pomidor et al. (2016). At the end of this process, we were able to select one specimen per species of *Brachycephalus* for which we computed clean surfaces needed for the automated procedures employed downstream in the geometric morphometric analyses (Pomidor et al., 2016).

2.3 | Three-dimensional geometric morphometric analysis of skull diversity in shape space

We used three methods to analyze skull diversity between the species of *Brachycephalus* in ordinated shape space. In the first method, we used a landmark-free method, the Generalized Procrustes Surface Analysis (GPSA; Pomidor et al., 2016), with the 3D surfaces reconstructed from high-resolution computed tomography. Generalized Procrustes Surface Analysis

Accepted Article

optimally superimposes multiple surfaces associating each point in one surface with its nearest neighbor on another surface (Pomidor et al., 2016). Multiple surfaces are superimposed to a designated mean (prototype) surface, which should be the most representative, least atypical species in the sample (Pomidor et al., 2016). We chose *B. ferruginus* as the designated mean (prototype) surface because the specimen was extremely well preserved, most representative in the sense that the majority of species of *Brachycephalus* are not hyperossified, and had no atypical morphometric features. The optimal superimposition for multiple surfaces is computed recursively by minimizing the Procrustes surface metric (PSM) between surfaces. PSM is a distance analogous to the Procrustes distance derived from Generalized Procrustes Analysis (Pomidor et al., 2016), which is used to quantify shape differences between species. Diversity in skull shape between the species of *Brachycephalus* was visualized as a three dimensional heat map. A heat map associates colors with the magnitude of variance measured at every point on the mean (prototype) surface with respect to the sample (Pomidor et al., 2016). The heat map is an effective way to graphically display shape variation in the sample (Pomidor et al., 2016). The color values are computed from the covariance matrix of the set of nearest neighbor points for each point on the mean (prototype) surface (Pomidor et al., 2016). Variance values are color coded, with blue and red indicating low and high values, respectively (Pomidor et al., 2016). All computations were carried out with the GPSA software package (Pomidor et al., 2016).

In the second method, we used Generalized Procrustes Analysis (GPA) with landmarks and curve and surface semilandmarks (hereafter, reference points [Reyment, 2010]), which were manually registered on the three-dimensional images of skulls of *Brachycephalus* generated with AVIZO. Reference points are depicted in Fig. 2 and described in Table 2. The coordinates for the reference points for the 18 species of *Brachycephalus* sampled here are available in the Supplementary Information S1. To establish geometric correspondence between

semilandmarks across the samples, the semilandmarks were allowed to slide along tangents in order to minimize the thin-plate spline bending energy between each individual skull and the sample average (Bookstein, 1997; Gunz et al., 2005; Gunz and Mitteroecker, 2013). Generalized Procrustes Analysis superimposes the original configurations of the reference points onto a single, global consensus configuration by carrying out three operations (Mitteroecker, 2020). First, differences in the position of the original configurations of the reference points are normalized by translation to a common centroid, computed as the average x , y , and z coordinates of all reference points of a configuration. Second, differences in size in the original configurations of reference points are normalized by scaling to an identical size, the unitary centroid size, defined as the square root of the summed squared distances between the reference points and their centroid. Third, the normalized and scaled reference points are optimally superimposed onto a mean (consensus) configuration so as to minimize the Procrustes distance, computed as the summed squared distances between corresponding reference points over all configurations. The size of each configuration of reference points was calculated as the centroid size, defined as the square root of the sum of squared distances of a set of reference points from their centroid. The Procrustes distances generated by GPA are global distances, which were used to compute differences in shape between the species of *Brachycephalus*. The sliding of semilandmarks was performed using the slider3d function from the R package Morpho version 2.8 (Schlager, 2017), whereas the GPA was computed using the procSym function in the same package.

In the third method, we relaxed the restriction of superimposition based on the Procrustes distances to a single, global consensus by using multiple, local consensuses (Von Zuben et al., in preparation). By using multiple, local consensuses the algorithm performs the superimposition taking into account the pattern of diversification in the skulls of *Brachycephalus*. The algorithm starts by computing the matrix of pairwise Procrustes distances among the reference points of

the 18 species of *Brachycephalus* using ordinary Procrustes analyses (Dryden and Mardia, 2016). Based on these distances, we computed a tree using the neighbor-joining (NJ) algorithm (Saitou and Nei, 1987). The NJ tree has $n = 18$ leaf nodes which correspond to the 18 species of *Brachycephalus* and $n - 2 = 16$ internal nodes. We estimated the hypothetical landmarks for the unobserved, internal nodes with the squared-change parsimony (SCP) algorithm (McArdle and Rodrigo, 1994), which minimizes the sum of squared internode differences, for all the coordinates of landmarks and semilandmarks across the entire tree. The NJ and SCP algorithms are computationally efficient and did not pose a significant impact on the whole computational burden. We still needed to perform n local Procrustes analyses, given the NJ tree composed of n leaf nodes. Therefore, given a reference node i for $i = 1, \dots, n$, we simply extracted from the NJ tree the local star tree having the i -th leaf node as one of its leaf nodes. This local star tree will always have three leaf nodes, one or two which will be internal nodes of the full tree, allowing for a very fast local Procrustes analysis. Although all the leaf nodes in the current local star tree have their corresponding reference points superimposed, only the reference node i will have the landmarks updated. Therefore, the proposal is iterative. Given the original skull reference points to be superimposed, we (1) obtained the distance matrix between them using the pairwise Procrustes distance; (2) applied the NJ algorithm to compute the binary tree for the current configuration of landmarks for the leaf nodes; (3) ran the SCP algorithm to compute the hypothetical landmarks and semilandmarks for the internal nodes of the tree; and finally (4) explored the hierarchical structure of the NJ tree to perform local Procrustes analysis for each one of the n leaf nodes. This sequence of steps is then repeated until convergence, measured by the amount of change in the landmarks and semilandmarks at the leaf nodes given the previous and the current iteration. The output of our algorithm includes the locally optimized landmarks and semilandmarks for the skull of the 18 species, the local Procrustes distances (1-Procrustes distances), and the corresponding NJ tree computed from the distances. Our method

has been implemented in MATLAB (Von Zuben et al., in preparation) and the convergence was always achieved with less than 20 iterations, considering a wide range of problems with a distinct number of leaf nodes (from tens to hundreds).

The PSM distances, the global Procrustes distances (g-Procrustes distances), and the local Procrustes distances (l-Procrustes distances) were then subjected to non-Metric Multidimensional Analysis (nmMDS; Mead, 1992). Non-Metric Multidimensional Analysis optimally projects distances and shape coordinates onto a lower dimensional space for visualization of the ordinated shape space and was computed using PAST 4.0 (Hammer et al., 2001).

2.4 | Three-dimensional geometric morphometric analysis of skull diversity in size-shape space

The covariance between shape and size in the skull of *Brachycephalus* was quantified using the landmarks, curve semilandmarks, and surface semilandmarks under the concept of allometry within the size-shape space formalism of geometric morphometrics (Dryden and Mardia, 2016; Mitteroecker et al., 2004). Under this formalism, interspecific allometric trajectories are calculated taking into account intraspecific allometries by computing a common allometric component (CAC), defined as $\mathbf{a} = (\mathbf{X}^t \mathbf{s}) / (\mathbf{s}^t \mathbf{s})$. Here, \mathbf{X} is the $n \times n$ matrix of shape coordinates derived from GPA and \mathbf{s} is the $n \times 1$ vector of centroid sizes on a logarithmic scale. The vector \mathbf{a} is normalized as $\mathbf{a}' = \mathbf{a} / \sqrt{\mathbf{a}^t \mathbf{a}}$. Visualization of allometric patterns is achieved by plotting scores of CAC against centroid size on a logarithmic scale (Mitteroecker et al., 2004). Residual shape components (RSC) are calculated by projecting out the common allometric component, computed as $\mathbf{W} = (\mathbf{I} - \mathbf{a}'(\mathbf{a}')^t)$. Residual shape components are the non-allometric shape components (Mitteroecker et al., 2004). Ordination of species in size-shape space was examined by plotting scores of the first residual component (RSC-1) against CAC (Mitteroecker et al., 2004). Diversity in skull morphology between species of *Brachycephalus* in size-shape space was

visualized as regionalized shape deformations representing spatial patterning (Bookstein, 1989; Mitteroecker et al., 2004). Deformation is computed with the thin-plate splines that interpolates surfaces over the reference points, minimizing the bending energy in analogy with the bending of an infinitely thin metal plate in continuum mechanics (Batra, 2006). All computations were performed with the CAC function in the R package Morpho (Schlager, 2017).

2.5 | Species tree estimation

Species tree estimation was performed using four mitochondrial genes, rRNA 12S, rRNA 16S, cytochrome c oxidase subunit I [COI], and cytochrome *b* [Cyt *b*]. We used 90 specimens of the 18 species of *Brachycephalus* sampled here (Table 1). Genomic DNA was extracted from liver (or muscle) tissue preserved in 100% ethanol (Clemente-Carvalho et al., 2015). Tissue samples were digested with proteinase K followed by a standard three-step phenol-chloroform extraction procedure (Green and Sambrook, 2013). Amplification via polymerase chain reaction (PCR) of the rRNA 12S, COI, and Cyt *b* genes was based on primers developed by Goebel et al. (1999). The rRNA 16S gene was amplified after Darst and Cannatella (2004). PCR amplification products were visualized on 1.0% agarose gels and purified using a QIAquick PCR Purification Kit (QIAGEN Inc., Venlo, The Netherlands). Purified PCR products were outsourced to MacroGen Inc. (Seoul, South Korea) for sequencing using the BigDye Terminator Kit and run on an ABI 3730xl DNA analyzer [Applied Biosystems, Inc., Grand Island, NY, USA]. Sequences were obtained in both directions with the same primers used for polymerase chain reaction amplification and subjected to BLAST searches (Altschul et al., 1997) in GenBank to determine that the target sequences had been amplified. All sequences were deposited in GenBank. Accession numbers are given in Supplementary Information S2. Sequence traces were analyzed using the phred program (Ewing et al., 1998). We obtained a total of 4826 base pairs (bp), of which 939, 1533, 1369, 985 bp were from the 12S rRNA, 16S rRNA, COI, and Cyt *b* genes, respectively. The authenticity of the COI and Cyt *b* genes was confirmed by amino acid

translation. Sequences were aligned using MAFFT (Katoh and Standley, 2013). We estimated a species tree for the species of *Brachycephalus* sampled here using the multi-species coalescent model implemented in BEAST 2.3 (Bouckaert et al., 2014). Sequence data containing the four mitochondrial genes were imported into BEAUti 2. Clock models and trees were linked across genes to ensure that mitochondrial genes shared the same evolutionary history. Site models were unlinked to allow for each gene to have its model of nucleotide substitution. Best-fitting DNA substitution models were selected according to the Akaike Information Criterion (AIC) in jModeltest 2.1.4 (Darriba et al., 2012). Model GRT + G was selected for rRNA 12S and rRNA 16S, TN93+G for COI, and HKY for Cyt *b*. The gamma distribution was estimated where needed from the data using four rate categories. Constant population size and strict clock (Drummond et al., 2006) were defined as priors. The calibrated Yule model, which is recommended for analyses using sequences from different species (Drummond and Bouckaert, 2015), was selected as prior. Two independent MCMC chains were run for 200 million generations each, sampling values every 100000 steps. Tracer files were examined using Tracer v1.7 (Rambaut et al., 2018). Convergence and stationarity were verified for model parameters by visual inspecting of marginal densities and effective sample sizes ($226 < ESS < 1801$) in Tracer v1.7 (Rambaut et al., 2018). The posterior trees were summarized in TreeAnnotator using common ancestor heights to obtain the maximum clade credibility tree. Trees were visualized and edited using FigTree v1.4.3 (Rambaut, 2016).

3 | RESULTS AND DISCUSSION

3.1 | Three-dimensional geometric morphometric analysis of skull diversity in shape space

The three skeletal states are distributed in the species of *Brachycephalus* as follows (Fig. 3). Non-hyperossified: *B. brunneus*, *B. didactylus*, *B. ferruginus*, *B. hermogenesi*, *B. izecksohni*, *B. pernix*, *B. pombali*, and *B. pulex*. Hyperossified bufoniform without dorsal shield: *B. alipioi*, *B. crispus*, *B. guarani*, *B. nodoterga*, *B. pitanga*, *B. toby*, and *B. vertebralis*. Hyperossified bufoniform with dorsal shield: *B. ephippium*, *B. garbeanus*, and *B. margaritatus*.

Skull diversity in the species of *Brachycephalus* in ordinated shape space was analyzed with three procedures. In the first procedure, which was fully automated, we superimposed the virtual surfaces of the skulls of *Brachycephalus* reconstructed from 3D microcomputed tomography using GPSA. In GPSA, the optimal superimposition of 3D surfaces is achieved by aligning the first and second longest axes of the surfaces, which are computed as the first two principal components of the array of 3D points making up the surfaces (Pomidor et al., 2016). This method failed, however, to correctly align the multiple 3D surfaces of *Brachycephalus*. We observed a similar outcome when we superimposed mandibles from several species of bats (Perez et al., personal observation). This suggests that the alignment algorithm used by GPSA is sensitive to objects whose major axes of variation are not well defined. Therefore, alternative algorithms will have to be devised to handle shapes that lack well defined major axes of variation. Here, we solved this problem by using instead the reconstructed images of the skull plus the vertebral column, which were then successfully superimposed using GPSA. The two other procedures we used were based on user-determined and manually registered reference points, although they differed in the superposition algorithm, which was global in one case and local in the other.

Diversity of skull shape in *Brachycephalus* is visualized in the ordinated space of the first two nmMDS axes (Fig. 4). Color polygons were drawn by hand and bound the four conditions of

skeletal states-baupläne, namely, non-hyperossified leptodactyliiform, non-hyperossified bufoniform, hyperossified bufoniform without dorsal shield, and hyperossified bufoniform with dorsal shield. Species of *Brachycephalus* in each of the four conditions of skeletal states-baupläne differ markedly in skull shape, as demonstrated by non-overlapping polygons computed from PSM, g-Procrustes, and l-Procrustes distance matrices (Fig. 4A,B,C). The marked dispersion in skull shape of the non-hyperossified leptodactyliiforms, *B. didactylus*, *B. hermogenesi*, and *B. pulex*, relative to species of *Brachycephalus* in the other three conditions of skeletal states, is noteworthy. This pattern emerges in the space of the first two nmMDS axes computed with landmarks using the g-Procrustes and l-Procrustes distance matrices (Fig. 4B,C). Differences in skull shape between the species of *Brachycephalus* relative to the prototype are visualized using GPSA as a three dimensional heat map (Fig. 5). In this map, the colors blue and red indicate low and high variance values, respectively. Differences in skull shape between the species of *Brachycephalus* involve primarily the frontoparietal and otic bones (Fig. 5).

3.2 | Three-dimensional geometric morphometric analysis of skull diversity in size-shape space

Skull diversity in the species of *Brachycephalus* is visualized in the ordinated size-shape space defined by RSC-1 and CAC (Fig. 6). Color polygons were drawn by hand and bound the four conditions of skeletal states-baupläne, namely, non-hyperossified leptodactyliiform, non-hyperossified bufoniform, hyperossified bufoniform without dorsal shield, and hyperossified bufoniform with dorsal shield. The pattern of skull diversity in *Brachycephalus* that emerges from the ordinated size-shape space is similar to that in the ordinated shape space (Figs. 4A,B,C; 6). That is, diversity in skull morphology amongst species of *Brachycephalus* is partitioned according to each of the four conditions of skeletal states-baupläne. Again, the outstanding outcome is the marked dispersion in skull morphology of the non-hyperossified leptodactyliiform species, *B. didactylus*, *B. hermogenesi*, and *B. pulex* in the space defined by the

common allometric component and the first residual component (Fig. 6). Another noticeable outcome is the partial overlap between non-hyperossified leptodactyliforms and non-hyperossified bufoniforms, which is caused by a single species, *B. didactylus* (Fig. 6). Because this result emerged in size-shape space rather than in shape space, we conjecture that interactions between size and shape unique to *B. didactylus* determine that the skull of this non-hyperossified leptodactyliform species is more similar to those of non-hyperossified bufoniform species (Fig. 6). We cannot however at this point offer any mechanistic explanation for this phenomenon.

The common allometric component scales linearly with size measured by the log of centroid size (Fig. 7). Consequently, the skull diversity of *Brachycephalus* that emerged in the ordinated size-shape space does not depart from allometry. That is, diversity in skull shape in *Brachycephalus* can be explained by allometry. Paluh et al. (2000) sampled all hyperossified frog genera and their sister lineages totaling 158 species and 145 genera of 54 anuran families, and detected no departure from allometry. Thus, this macroevolutionary trend for anurans appears to hold for the case of the relatively smaller *Brachycephalus* radiation. Shape variation in the skull of *Brachycephalus* as a function of size, that is, allometry, is modelled as deformation in the size-shape formalism (Mitteroecker et al., 2004). Deformation shows that in the direction of increasing size, the common allometric component consists of a marked broadening of the frontoparietal bones in the skull vault and a postero-lateral displacement of the otic bones in the otic region (Fig. 7). Paluh et al. (2020) identified the relative length and width of the frontoparietal bones as a factor driving shape differences in the skull of all hyperossified frog genera. At a larger evolutionary scale, Bardua et al. (2020) also identified the frontoparietal and otic bones as part of 13 modules of 19 cranial regions in their analysis of the frog skull. Whereas there is an approximately linear relationship between skull shape and size, the same is not true of the relationship between hyperossification and size (Figs. 7, 8). The degree of

hyperossification in *Brachycephalus* does not increase monotonically with increasing body size, as non-hyperossified bufoniform species and hyperossified bufoniform species without dorsal shield do share identical mean body sizes (Fig. 8).

3.3 | Robustness of pattern of skull diversity as a function of data acquisition and statistical formalism

High-resolution 3D microcomputed tomography imaging in connection with 3DGM revealed that the species of *Brachycephalus* differ in skull morphology. Furthermore, the differences are associated with the four conditions of skeletal states-baupläne (Figs. 4, 6, 7). This pattern is to a large extent independent of the algorithm of superposition, whether global or local, and of data acquisition that is, automated, landmark-free or manually registered, landmark-based.

Automated landmark-free methods sample phenotypes intensively and generate high-dimensional data (Gao et al., 2018). Conversely, such intensive sampling is not achieved by user-defined methods that rely on manually registered reference points. Nevertheless, methods such as the GPSA that use automated virtual surfaces generate maps between surfaces that lack the pointwise homology of user-defined landmarks (Pomidor et al., 2016). That is, they lack transitivity, which yields global consistency of pairwise mappings between surfaces (Gao et al., 2018). This problem is addressed in GPSA by optimally associating points in different surfaces with their nearest neighbors (Pomidor et al., 2016). Consequently, a relevant question is whether 3DGM analyses predicated on user-based or automated methods of data gathering yield ordinated shape spaces that are mutually consistent (Gao et al., 2018). Furthermore, as pointed out by Gao et al. (2018), GPSA may produce a Y pattern of interspecific ordination. Here, however, the ordinated shape space generated by GPSA did not produce a Y pattern of interspecific ordination (Fig. 4A). The landmark-free automated method thus behaved as well as the manually registered, landmark-based method.

Accepted Article

However, we must point out that the larger diversity in skull morphology of the non-hyperossified leptodactyliform species, *B. didactylus*, *B. hermogenesi*, and *B. pulex*, relative to that of species of *Brachycephalus* in the other three conditions of skeletal states-baupläne, emerged only from the landmarks-based dataset. This finding is relevant because landmarks defined by experienced morphometricians are regarded as providing a “ground truth” with respect to the derived ordinated size and/or size-shape space (Gao et al., 2018; Gao et al., 2019). Therefore, the landmark-based method of data acquisition will likely remain relevant as a tool to reveal morphological variability and diversity.

3.4 | Species tree estimation

Our mitochondrial species tree revealed that *B. pulex* is sister to all species of *Brachycephalus* (Fig. 9). Next in the branching order, *B. brunneus*, *B. ferruginus*, *B. izecksohni*, *B. pernix*, and *B. pombali* are monophyletic. This lineage is the sister to all other species and *B. hermogenesi* is the sister to the remaining species. *Brachycephalus didactylus* is sister to two monophyletic lineages. One lineage includes *B. ephippium*, *B. garbeanus*, and *B. margaritatus*. The other monophyletic lineage includes *B. alipioi*, *B. crispus*, *B. guarani*, *B. nodoterga*, *B. pitanga*, *B. toby*, and *B. vertebralis*. Earlier, Clemente-Carvalho et al. (2011) estimated a species tree for *Brachycephalus* based on mitochondrial genes that sampled a single specimen per species, which yielded a trichotomy with many branches lacking adequate support, as measured by posterior probabilities. Our current species tree, which sampled multiple individuals per species, resolved the phylogenetic relationships between the species of *Brachycephalus* sampled here reasonably well. Our mitochondrial species tree implies the following about the evolution of the conditions of skeletal states-baupläne in *Brachycephalus*. First, the non-hyperossified skeletal state is the ancestral condition for *Brachycephalus*. Second, the hyperossified skeletal state evolved once in *Brachycephalus*, with the appearance of a dorsal shield in the lineage leading to *B. ephippium*, *B. garbeanus*, and *B. margaritatus*. Third, the leptodactyliform bauplan is the ancestral condition for

Brachycephalus, whereas the bufoniform bauplan evolved twice independently in *Brachycephalus*. Recently, Condez et al. (2020) demonstrated quantitatively that the non-hyperossified skeletal state is indeed the ancestral skeletal state in *Brachycephalus*.

The most striking result, however, is the lack of monophyly of the non-hyperossified leptodactyliiform species of *Brachycephalus*. Condez et al.'s (2020) also demonstrated the same result with their mitochondrial species tree. The branching order of the non-hyperossified leptodactyliiform species differs though between Condez et al.'s (2020) and our mitochondrial species trees (present work). In Condez et al.'s (2020) mitochondrial species tree *B. hermogenesi* is the sister taxon to all other *Brachycephalus*, whereas *B. pulex* is the sister taxon in our species tree. Remarkably, the phylogenetic diversity of the non-hyperossified leptodactyliiform revealed by the mitochondrial species tree is mirrored by our analysis of the diversity in skull morphology in shape and size-shape space (Figs. 4, 6, 9). Skull diversity in the non-hyperossified leptodactyliiform species of *Brachycephalus* is markedly larger when compared to skull diversity in species in the other three conditions of skeletal states-bauplane. The diversity of non-hyperossified leptodactyliiforms is not limited, however, to skull morphology or molecular phylogenetic branching patterns. Recently, Condez et al. (2016) described a fourth species of non-hyperossified leptodactyliiform, *B. sulfuratus* and, in addition, discovered three putative new species of non-hyperossified leptodactyliiforms based on their magnitude of molecular variation (Condez et al., 2020). *Brachycephalus sulfuratus* extended the distribution of the non-hyperossified leptodactyliiform species from the State of Bahia in Northeastern Brazil (Napoli et al., 2011) into the State of Santa Catarina in Southern Brazil (Condez et al., 2016). The discovery of *B. sulfuratus* revealed that the geographic distribution of the non-hyperossified leptodactyliiform species is larger than the distribution of any of the three other conditions of skeletal states-bauplane.

The non-hyperossified leptodactyliform condition thus emerges as evolutionarily complex in terms of morphological, molecular diversity, and geographic distribution. Therefore, additional morphological, molecular, and distributional data for the non-hyperossified leptodactyliform skeletal state-baupläne condition will be needed to further understand the evolutionary history of *Brachycephalus*.

ACKNOWLEDGEMENTS

Caio M. S. F. F. dos Santos is supported by a doctoral scholarship from Conselho Nacional de Desenvolvimento Científico e Tecnológico (CNPq; 141467/2019-3). P. R. Laborda is supported by a postdoctoral fellowship from CAPES (PNPD20131756). R. T. Lopes is partially supported by a research fellowship from CNPq. The assistance of Ana Claudia Reis Alves, Vinícius Bonato, Ricardo J. Sawaya, Glauco Machado, and Ariovaldo A. Giaretta in several phases of this project is most sincerely appreciated. Isabel Moura Miller and David Miller were most gracious with their time and hospitality at Macaé de Cima, Rio de Janeiro. We are deeply indebted to Célio F. B. Haddad for making available the images of *Brachycephalus*. We are grateful to the following curators, collection managers, and institutions that loaned us specimens for this study. Ulisses Caramaschi, José R. Pombal Jr., Manoela Woitovicz Cardoso, Pedro H. Pinna, Museu Nacional, Rio de Janeiro; Victor G. Dill Orrico, Tadeu Medeiros, Universidade Estadual de Santa Cruz, Bahia; Célio Fernando Baptista Haddad, Nadya Pupin, Mariana Lyra, Universidade Estadual Paulista, Rio Claro, São Paulo; Mirco Solé Kienle, Iuri Ribeiro Dias, Universidade Estadual de Santa Cruz, Bahia; Luís Felipe de Toledo Ramos Pereira, Michela Borges, Karina Rebelo Gomes, Museu de Zoologia da Universidade Estadual de Campinas “Adão José Cardoso”, São Paulo, Brazil. Thaís H. Condez kindly made available samples of *B.*

crispus, *B. hermogenesi*, and *B. nodoterga*. Two anonymous reviewers made substantial contributions that greatly improved the conception and clarity of the manuscript.

CONFLICT OF INTEREST

The authors declare no potential conflicts of interest with respect to the authorship and/or publication of this article.

LITERATURE CITED

- Altschul SF, Madden TL, Schaffer AA, Zhang J, Zhang Z, Miller M, Lipman DJ. 1997. Gapped BLAST and PSI-BLAST: a new generation of protein database search programs. *Nucleic Acids Res* 25:3389–3402.
- Bardua C, Fabre AC, Bon M, Das K, Stanley EL, Blackburn DC, Goswami A. 2020. Evolutionary integration of the frog cranium. *Evolution* 74:1200–1215.
- Batra RC. 2006. *Elements of continuum mechanics*. Virginia: Reston.
- Bookstein FL. 1989. Principal warps: Thin plate splines and the decomposition of deformations. *IEEE T Pattern Anal* 11:567–585.
- Bookstein FL. 1997. *Morphometric tools for landmark data*. Cambridge: Cambridge University Press.
- Bouckaert R, Heled J, Kühnert D, Vaughan T, Wu CH, Xie D, ... Drummond AJ. 2014. BEAST 2: A software platform for Bayesian evolutionary analysis. *PLoS Comput Biol* 15(4):e1006650.
- Cardini A. 2020. Modern morphometrics and the study of population differences: Good data behind clever analyses and cool pictures? *Anat Rec* 303:1–19.
- Clarke BT. 1996. Small size in amphibians: its ecological and evolutionary implications. *Symp Zool Soc Lond* 69:201–224.
- Clemente-Carvalho RBG, Antoniazzi M, Jared C, Haddad CFB, Alves ACR, Rocha HS, ... Reis SF. 2009. Hyperossification in miniaturized toadlets of the genus *Brachycephalus* (Amphibia: Anura: Brachycephalidae): Microscopic structure and macroscopic patterns of variation. *J Morph* 270:1285–1295.
- Clemente-Carvalho RBG, Klaczko J, Perez SI, Alves ACR, Haddad CFB, Reis SF. 2011. Molecular phylogenetic relationships and phenotypic diversity in miniaturized toadlets, genus *Brachycephalus* (Amphibia: Anura: Brachycephalidae). *Mol Phyl Evol* 61:79–89.
- Clemente-Carvalho RBG, Perez SI, Tonhatti, CH, Condez TH, Sawaya RJ, Haddad CFB, Reis SF. 2015. Boundaries of morphological and molecular variation and the distribution range of a miniaturized froglet, *Brachycephalus nodoterga* (Anura: Brachycephalidae). *J Herp* 50:169–178.

- Condez TH, Haddad CFB, Zamudio KR. 2020. Historical biogeography and multi-trait evolution in miniature toadlets of the genus *Brachycephalus* (Anura: Brachycephalidae). *Biol J Linn Soc* 129:664–686.
- Darriba D, Taboada GL, Doallo R, Posada D. 2012. jModelTest 2: more models, new heuristics and parallel computing. *Nat Methods* 9:772.
- Darst CR, Cannatella DC. 2004. Novel relationships among hyloid frogs inferred from 12S and 16S mitochondrial DNA sequences. *Mol Phyl Evol* 31:462–475.
- Drummond AJ, Bouckaert RR. 2015. *Bayesian evolutionary analysis with BEAST*. Cambridge: Cambridge University Press.
- Drummond AJ, Ho SYW, Phillips MJ, Rambaut A. 2006. Relaxed phylogenetics and dating with confidence. *PLoS Biol* 4(5):e88.
- Dryden IL, Mardia KV. 2016. *Statistical shape analysis: With applications in R*. Hoboken: Wiley Press.
- Ewing B, Hillier L, Wendl MC, Green P. 1998. Base-calling of automated sequencer traces using phred. I. Accuracy assessment. *Gen Res* 8:175–185.
- Fish JL. 2017. Evolvability of the vertebrate craniofacial skeleton. *Semin Cell Dev Biol* 17:30284–30287.
- Frost D.R. 2020. Amphibian species of the world: An online reference. Version 6.1 (Date of access). Electronic Database accessible at <https://amphibiansoftheworld.amnh.org/index.php>. American Museum of Natural History, New York, USA.
- Gao T, Yapuncich GS, Daubechies I, Mukherjee S, Boyer DM. 2018. Development and assessment of fully automated and globally transitive geometric morphometric methods, with application to a biological comparative dataset with high interspecific variation. *Anat Rec* 301:636–658.
- Gao T, Kovalsky SZ, Boyer DM, Daubechies I. 2019. Gaussian process landmarking for three-dimensional geometric morphometrics. *SIAM J Math Data Sci* 1:237–267.
- Goebel AM, Donnelly JM, ATZ ME. 1999. PCR primers and amplification methods for 12S ribosomal DNA, the control region, cytochrome oxidase I, and cytochrome *b* in bufonids and other frogs, and an overview of PCR primers which have amplified DNA in amphibians successfully. *Mol Phyl Evol* 11:163–199.
- Green MR, Sambrook J. 2013. *Molecular cloning: A laboratory manual*. Huntington: Cold Spring Harbor Laboratory Press.
- Gunz P, Mitteroecker P. 2013. Semilandmarks: a method for quantifying curves and surfaces. *Hystrix* 24:103–109.
- Gunz P, Mitteroecker P, Bookstein FL. 2005. Semilandmarks in three dimensions. In Slice DE, editor. *Modern morphometrics in physical anthropology*. New York: Kluwer Academic/Plenum Publishers. p 73–98.

- Hammer Ø, Harper DAT, Ryan PD. 2001. PAST: paleontological statistics software package for education and data analysis. *Palaeontol Electron* 4:1–9.
- Handigran GR, Wassersug RJ. 2007. The anuran Bauplan: a review of the adaptive, developmental, and genetic underpinnings of frog tadpole morphology. *Biol Rev* 82:1–25.
- Hanken J. 1993. Adaptation of bone growth to miniaturization of body size. In: Hall BK, editor. *Bone growth – B*. Boca Raton: CRC Press. p 79–104.
- Hanken J, Wake DB. 1993. Miniaturization of body size: Organismal consequences and evolutionary significance. *Annu Rev Ecol Syst* 24:501–519.
- Katoh K, Standley DM. 2013. MAFFT Multiple Sequence Alignment Software Version 7: Improvements in performance and usability. *Mol Biol Evol* 30:772–780.
- Klingenberg CP. 2016. Size, shape, and form: concepts of allometry in geometric morphometrics. *Dev Genes Evol* 226:113–137.
- McArdle B, Rodrigo AG. 1994. Estimating the ancestral states of a continuous-valued character using squared-change parsimony: An analytical solution. *Sys Bio* 43:573–578.
- Mead A. 1992. Review of the development of multidimensional scaling methods. *J R Stat Soc B* 41:27–39.
- Mitteroecker P. 2020. Morphometrics in evolutionary developmental biology. In: Nuño de la Rosa L, Müller GB. editors. *Evolutionary developmental biology*. Cham: Springer Nature. p 1–11.
- Mitteroecker P, Gunz P, Bernhard M, Schaefer K, Bookstein FL. 2004. Comparison of cranial ontogenetic trajectories among great apes and humans. *J Hum Evol* 46:679–698.
- Napoli MF, Caramaschi U, Cruz CAG, Dias IR. 2011. A new species of flea-toad, genus *Brachycephalus* Fitzinger (Amphibia: Anura: Brachycephalidae), from the Atlantic rainforest of southern Bahia, Brazil. *Zootaxa* 2739:33–40.
- Paluh DJ, Stanley EL, Blackburn DC. 2020. Evolution of hyperossification expands skull diversity in frogs. *Proc Natl Acad Sci (USA)* 117:8554–8562.
- Pomidor BJ, Makedonska J, Slice DE. 2016. A landmark-free method for three-dimensional shape analysis. *PLoS ONE* 11(3):e0150368.
- Rambaut A. 2016. FigTree v1.4.3: Tree figure drawing tool. <http://tree.bio.ed.ac.uk/software/figtree/>
- Rambaut A, Drummond AJ, Xie D, Baele G, Suchard MA. 2018. Posterior summarization in Bayesian phylogenetics using Tracer 1.7. *Syst Biol* 67:901–904.
- Rannala B, Edwards SV, Leaché A, Yang Z. 2020. The multi-species coalescent model and species tree inference. In: Scornavacca C, Delsuc F, Galtier N, editors. *Phylogenetics in the genomic era*. Authors open access book. p 1–21.
- Reyment R. A. 2010. Morphometrics: An historical essay. In: Elewa AMT, editors. *Morphometrics for nonmorphometricians*. New York: Springer Verlag. p. 9–24.
- Rittmeyer EN, Allison A, Gründler MC, Thompson DK, Austin CC. 2012. Ecological guild evolution and the discovery of the world’s smallest vertebrate. *PLoS ONE* 7(1): e29797.

- Saitou N, Nei M. 1987. The Neighbor-Joining method – a new method for reconstructing phylogenetic trees. *Mol Biol Evo* 4:406–425.
- Schlager S. 2017. “Morpho and Rvcg – Shape Analysis in R.” In Zheng G, Li S, Székely G, editors. *Statistical shape and deformation analysis*. New York: Academic Press. p 217–256.
- Trueb L. 1973. Bones, frogs, and evolution. In: Vial JL, editor. *Evolutionary biology of the anurans: Contemporary research on major problems*. Columbia: University of Missouri Press. p 65–132.
- Trueb L, Alberch P. 1985. Miniaturization and the anuran skull: a case study of heterochrony. In: Duncker HR, Fleischer G, editors. *Functional morphology of vertebrates*. Stuttgart: Gustav Fisher Verlag. p 113–121.
- Von Zuben FJ, Reis SF, Perez SI. 2020. Multiple Procrustes alignment of landmark configurations on a phylogenetic tree. In preparation.
- Yang LM, Ornitz DM. 2019. Sculpting the skull through neurosensory epithelial-mesenchymal signaling. *Dev Dynam* 248:88–97.

Figure legends

Fig. 1. Images of *Brachycephalus*. From left to right (top to bottom). Leptodactyliform species: *B. hermogenesi*. Bufoniform species: *B. mariaeterezae*, *B. albolineatus*, *B. garbeanus*, *B. pitanga*, and *B. toby*. Images not to scale.

Fig. 2. Dorsal (A) and ventral (B) three-dimensional microcomputed tomography images views of the skull of *Brachycephalus pernix* with locations of landmarks (red), surface semilandmarks (green), and contour semilandmarks (blue). The lower jaw was digitally removed for better visualization.

Fig. 3. Three-dimensional digital reconstruction of the skeleton of *Brachycephalus* based on high-resolution computed tomography. Dorsal view. Non-hyperossified: *B. brunneus*, *B. didactylus*, *B. ferruginus*, *B. hermogenesi*, *B. izecksohni*, *B. pernix*, *B. pombali*, and *B. pulex*. Hyperossified without dorsal shield: *B. alipioi*, *B. crispus*, *B. guarani*, *B. nodoterga*, *B. pitanga*, *B. toby*, *B. vertebralis*. Hyperossified with dorsal shield: *B. ephippium*, *B. garbeanus*, *B. margaritatus*.

Fig. 4. Ordinated shape space for the species of *Brachycephalus* derived from non-metric multidimensional scaling. (A) Global superimposition of automated virtual surfaces. (B) Global superimposition of manually registered reference points. (C) Local superimposition of manually registered reference points. Orange, red, green, and blue polygons bound non-hyperossified leptodactyliform species, non-hyperossified bufoniform species, hyperossified bufoniform species without dorsal shield, and hyperossified bufoniform species with dorsal shield, respectively.

Fig. 5. Variation in skull shape between species of *Brachycephalus* relative to the prototype visualized as a three dimensional heat map derived from the virtual surfaces using GPSA (Pomidor et al., 2016). Blue and red colors indicates low and high values of shape variation, respectively, from the designated, mean prototype surface, *Brachycephalus ferruginus*.

Fig. 6. Common allometric component scores plotted against the first residual shape scores for *Brachycephalus*. Orange, red, green, and blue polygons bound non-hyperossified leptodactyliform species, non-hyperossified bufoniform species, hyperossified bufoniform species without dorsal shield, and hyperossified bufoniform species with dorsal shield, respectively.

Fig. 7. Log centroid size plotted against the common allometric component scores for *Brachycephalus*. Three dimensional images of the skull of *Brachycephalus* show changes in shape as a function of the increase in the common allometric component. Orange, red, green, and blue polygons bound non-hyperossified leptodactyliform species, non-hyperossified bufoniform species, hyperossified bufoniform species without dorsal shield, and hyperossified bufoniform species with dorsal shield, respectively.

Fig. 8. Hyperossification in *Brachycephalus* as a function of increasing body size. Images not to scale.

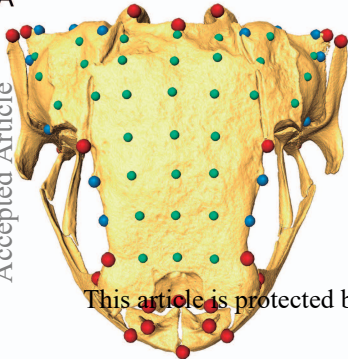
Fig. 9. Species tree for *Brachycephalus* estimated with the multispecies coalescent model using four mitochondrial DNA genes. Black circles denote posterior probability values > 0.95.



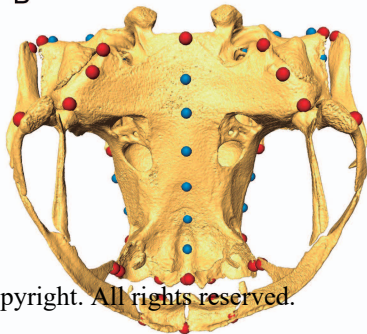
This article is protected by copyright. All rights reserved.

A

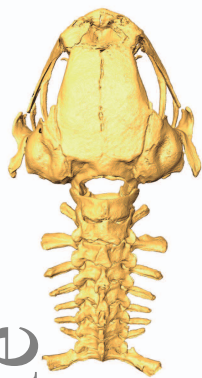
Accepted Article



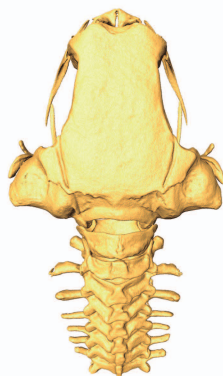
B



This article is protected by copyright. All rights reserved.



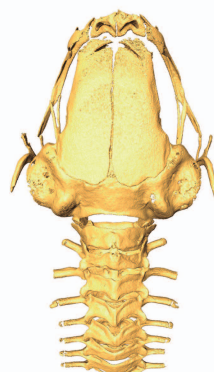
B. brunneus



B. didactylus



B. ferruginus



B. hermogenesi



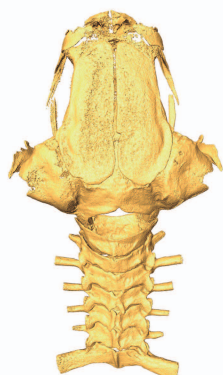
B. izecksohni



B. pernix



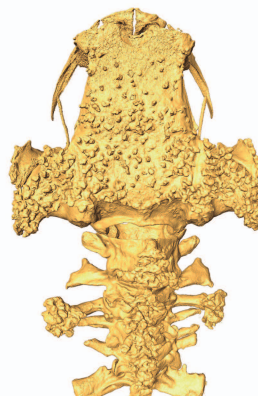
B. pombali



B. pulex



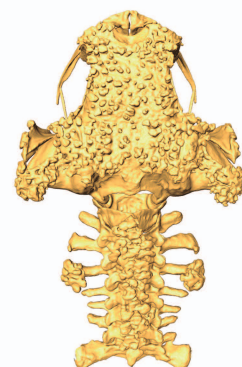
B. alipioi



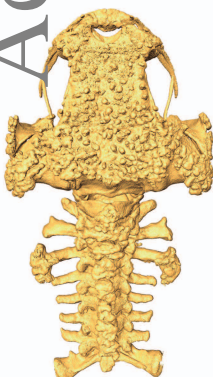
B. crispus



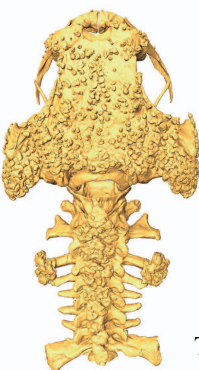
B. guarani



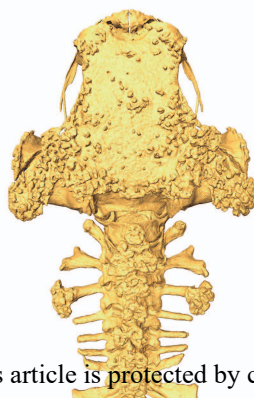
B. nodoterga



B. pitanga



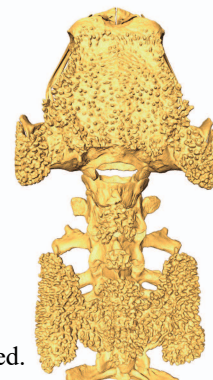
B. toby



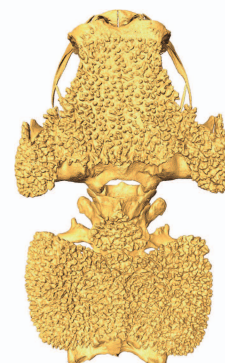
B. vertebralis



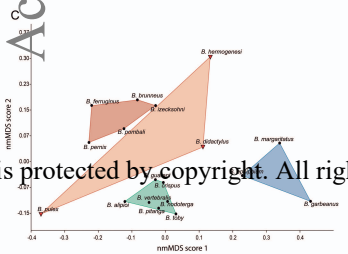
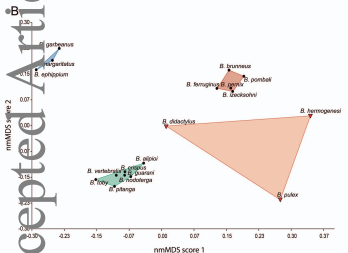
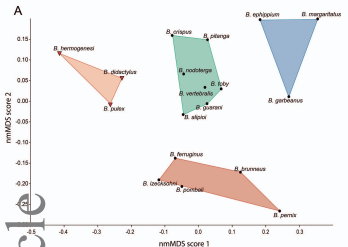
B. ehippium

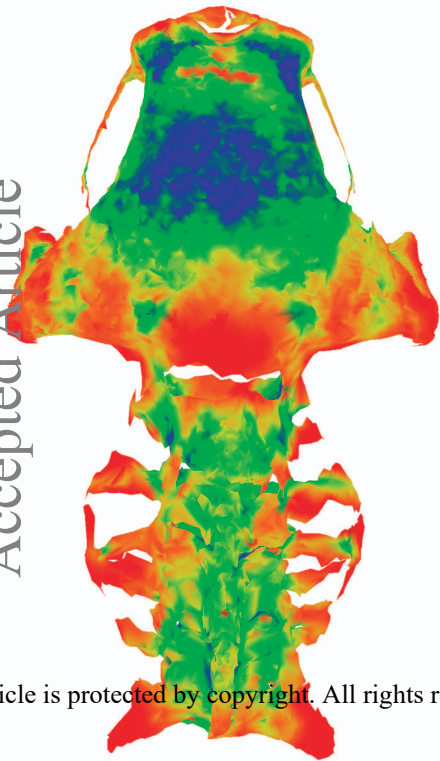


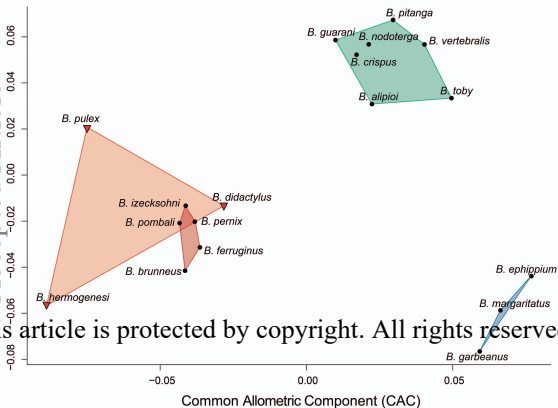
B. garbeanus

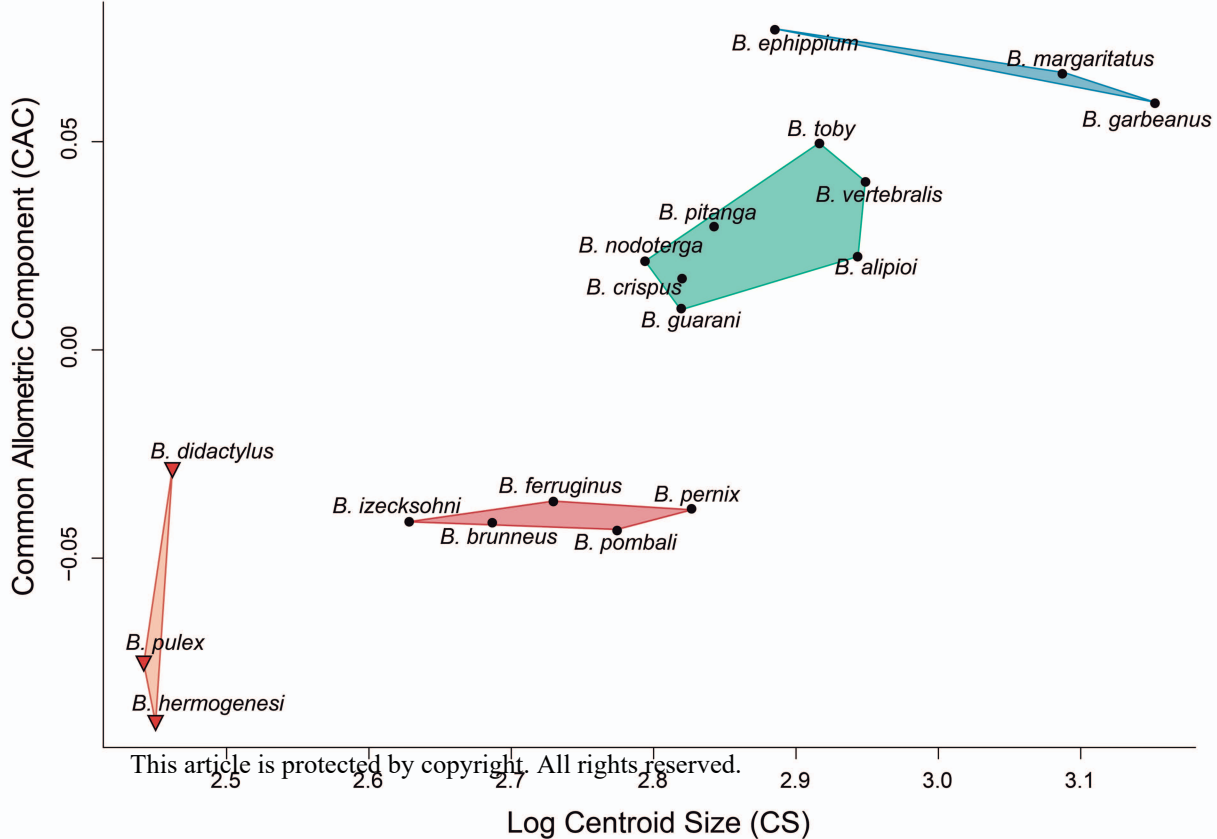


B. margaritatus







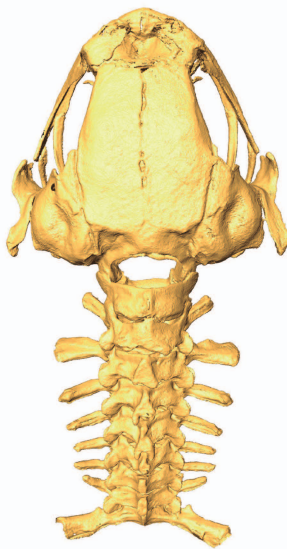


Non-hyperossified
leptodactyliform species



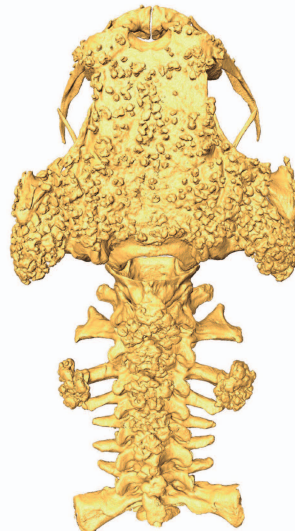
\bar{x} Body size = 9.14 (± 0.86)

Non-hyperossified
bufoniform species



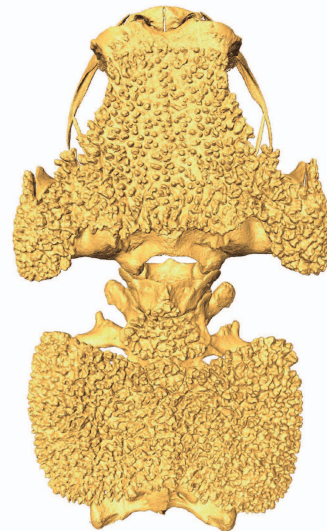
\bar{x} Body size = 12.40 (± 1.73)

Hyperossified bufoniform
species without dorsal shield



\bar{x} Body size = 12.59 (± 1.64)

Hyperossified bufoniform
species with dorsal shield



\bar{x} Body size = 18.10 (± 1.02)

This article is protected by copyright. All rights reserved.
Increasing body size and degree of hyperossification



